Electrochimica Acta 330 (2020) 135200

Contents lists available at ScienceDirect

Electrochimica Acta

journal homepage: www.elsevier.com/locate/electacta

Microwave-assisted high-yield exfoliation of vanadium pentoxide nanoribbons for supercapacitor applications

Ya Chen [a, b, *], Kamalambika Muthukumar [b], Levon Leban II [b], Jun Li [b, **]

[a] School of Metallurgy and Environment, Central South University, Changsha, 410083, China
[b] Department of Chemistry, Kansas State University, Manhattan, KS, 55606, USA

ARTICLE INFO

Article history:
Received 12 August 2019
Received in revised form
12 October 2019
Accepted 3 November 2019
Available online 6 November 2019

Keywords:
Supercapacitor
Vanadium pentoxide
Electrode material
Nanoribbons
Microwave-assisted exfoliation

ABSTRACT

Ultrathin 2D transition metal oxide materials have great advantages as electrical energy storage materials. At present, improving the yield and processing techniques is one of the top priorities to push these materials for scalable applications. Here, a novel microwave-assisted technique is presented to exfoliate crystalline α-V_2O_5 powder into wrinkled nanoribbons. The yield of the V_2O_5 nanoribbons can reach up to 20% after 40 min of microwave treatment. The as-exfoliated V_2O_5 nanoribbons are further used to form a strongly bound hybrid material with larger graphene oxide (GO) nanosheets through a simple cation-mediated self-assembly process, and the 2D GO template is converted into highly conductive reduced graphene oxide (rGO) nanosheets by thermal annealing treatment. The obtained V_2O_5/rGO hybrid material exhibits typical capacitive behavior with a specific capacitance of 423.6 F g^{-1} at 1 A g^{-1}, an excellent high-rate capability and good cycling stability. These results suggest the exciting potential of the microwave-assisted technique for high-yield exfoliation of V_2O_5 nanoribbons toward future electrical energy storage applications.

1. Introduction

The rapid consumption of fossil fuels in energy production and the associated climate issues have led to urgent demands for the development of sustainable energy supplies throughout the world. While the quantity of energy generated from renewable sources, including solar radiation, hydropower and wind, has increased steadily over the past years, their utilization is limited by the large fluctuations in electric power generation. Efficient energy storage systems are thus needed to mitigate this problem and supply the world with the renewable energy on demand [1–3]. Among various energy storage systems, supercapacitors bridging the gap between batteries and conventional capacitors have attracted great attention [4,5]. In addition, supercapacitors exhibit a number of highly desired features such as high power density, superior cycle life and high reliability. However, the energy density of supercapacitors is much lower than that of commercial batteries [6–10]. To overcome this limitation, considerable efforts have been devoted to the creation of new electrode materials for supercapacitors. Compared with common carbon-based electrode materials which only use the electrical double-layers at the electrode/electrolyte interface for charge storage, transition metal oxides can make use of both the electrical double-layers and the reversible redox reactions on the surface or subsurface of electrodes for charge storage, offering much higher specific capacitances. During the past years, various transition metal oxides, such as RuO_2, MnO_2, Fe_2O_3, NiO and $NiCo_2O_4$, have been extensively investigated as the electrode materials for supercapacitors [11–15].

Among the numerous transition metal oxides investigated, vanadium pentoxide (V_2O_5) is considered as one of the most promising pseudocapacitive electrode materials due to its natural abundance, low cost, unique layered structure and high theoretical capacitance. To date, plenty of V_2O_5 materials have been successfully synthesized for supercapacitors. In particular, nanostructured V_2O_5 materials have attracted much attention because their unique morphologies and structures were expected to provide both high surface areas for fast redox reactions and facile paths for electrolyte diffusion associated with the energy storage processes. However, the nanostructured materials were usually synthesized by similar hydrothermal processes, hydrothermal treatment of a $[VO_2]^+$-contained solution derived from the reaction between V_2O_5

* Corresponding author. School of Metallurgy and Environment, Central South University, Changsha, 410083, China.
** Corresponding author.
E-mail addresses: chenya_mes@csu.edu.cn (Y. Chen), junli@ksu.edu (J. Li).

https://doi.org/10.1016/j.electacta.2019.135200
0013-4686/

powder and a H_2O_2 solution. As a result, most of the nanostructured V_2O_5 exhibited just a nanowire or nanorod morphology with a bilayer structure [16–18]. Among these nanostructured V_2O_5, the V_2O_5 nanowires anchored on N-doped graphene were reported to deliver a high specific capacitance, but their clearly battery-like behavior indicated that the capacitance should be derived from insertion charge storage [16]. Although V_2O_5 nanospheres synthesized through hydrothermal treatment of an ammonium metavanadate solution or pyrolysis of a vanadium (V) tri-isopropoxide oxide mixture have recently been reported to show typical capacitive behavior, they were mainly embedded in graphene nanosheets or coated on carbon-xerogel microspheres with a low mass loading (10–30%), and thus the obtained hybrid materials exhibited a low specific capacitance [19,20]. Considering that the capacitive performance of V_2O_5 is mainly hindered by its electronic and ionic conductivities, a delicate design of the nanostructured hybrid materials should be needed to independently tailor the electronic and ionic transport pathways and thus further improve the performance of the electrodes [21,22].

Recently, ultrathin 2D materials have gained great interests as energy storage materials due to their unique physicochemical characteristics [23]. In most cases, these atomically thin 2D materials were derived from exfoliation of bulk materials with layered structures, such as hexagonal boron nitride (h-BN), transition metal dichalcogenides (TMDs), layered metal oxides, etc. [24–28]. Similarly, V_2O_5 also has a layered structure comprised of distorted VO_6 octahedra [29]. The adjacent layers are just stacked together via weak van der Waals interactions, suggesting the possibility of exfoliating the bulk powder into ultrathin nanosheets by liquid exfoliation. Indeed, Rui et al. [30]. first produced the ultrathin V_2O_5 nanosheets by liquid exfoliation. In the process of exfoliation, the V_2O_5 powder was first soaked in a formamide solution for one night and then sonicated for 3 days. The exfoliated V_2O_5 nanosheets were separated from the dispersion and processed into composite electrodes by a conventional method. Recently, Zhang et al. [31]. reported another procedure for liquid exfoliation of V_2O_5 into nanosheets by directly sonicating V_2O_5 powder dispersed in water for 5 h. But the results showed that the concentration of nanosheets in the obtained supernatant was only 0.19 mg mL^{-1} and the total yield of the nanosheets was just about 3.8%. While the V_2O_5 nanosheets obtained under both conditions exhibited good electrochemical performance, it is noteworthy that the production procedures based on liquid exfoliation were time-consuming with low yield and thus could be less competitive for practical applications. To the best of our knowledge, the low yield (or productivity) is still a universal and critical challenge for preparation of ultrathin V_2O_5 nanosheets and other 2D materials. In addition, the electrical conductivity of V_2O_5 nanosheets is low, limiting the electrode performance at high charge-discharge rates.

Herein, we demonstrate a novel microwave-assisted technique to exfoliate V_2O_5 powder into wrinkled nanoribbons. The yield of the nanoribbons can reach up to 20% after 40 min of exfoliation. To improve their electrochemical performance at high charge-discharge rates, the as-prepared V_2O_5 nanoribbons were used to form a strongly bound hybrid material with well dispersed graphene oxide (GO) nanosheets through a simple self-assembly process, and the GO nanosheets were further converted into highly conductive reduced graphene oxide (rGO) nanosheets by a thermal annealing process. Such V_2O_5/rGO hybrid materials exhibit typical capacitive behavior in the potential range of −0.95–0.1 V with a specific capacitance of 423.6 F g^{-1} at 1 A g^{-1}. The symmetric supercapacitor based on the hybrid material shows a high energy density of 58.8 Wh kg^{-1} at an average power density of 500 W kg^{-1}, an excellent high-rate capability and good cycling stability over 2000 cycles. These encouraging results demonstrate the great potential of the microwave-assisted technique for rapid high-yield production of V_2O_5 nanoribbons in energy storage applications.

2. Experimental section

All reagents were analytical grade and were directly used without further purification.

2.1. Microwave-assisted exfoliation of bulk V_2O_5

In a typical procedure, bulk V_2O_5 powder (350 mg, Acres Organic) was first soaked in DI water for 4 h. After the water was removed by centrifugation, the powder was then transferred into a 10 mL glass vessel containing 7 mL tetrahydrofuran (THF, Fisher Chemical) to form a suspension. The suspension was put in a microwave system (CEM Corporation) and treated for 40 min (300 W, 150 °C, 15 bar). After the microwave treatment, the THF solvent was removed by centrifugation and the powder was washed with DI water to remove the residual THF. Finally, the microwave-treated powder was dispersed in 14 mL DI water and sonicated for 15 min.

After the ultrasonic treatment, the exfoliated V_2O_5 nanoribbons were isolated from the supernatant via centrifugation. The supernatant contained 4.9 mg mL^{-1} of V_2O_5 nanoribbons and 0.8 mg mL^{-1} of dissolved V_2O_5. The yield of V_2O_5 nanoribbons was about 20%, which was determined by the weight percentage of the dried exfoliated V_2O_5 nanoribbons relative to the starting bulk V_2O_5 powder.

2.2. Preparation of V_2O_5/rGO

The obtained V_2O_5 nanoribbon supernatant (14 mL) was mixed with graphene oxide (GO, ACS Material) to form a suspension with a V_2O_5-to-GO weight ratio of 8:2. The suspension was sonicated for 30 min to ensure that the GO nanosheets were dispersed and mixed with the V_2O_5 nanoribbons homogeneously. Then 1 mL of 0.1 M Na_2SO_4 solution was added into the suspension, which neutralized the charges and led to self-assembly of V_2O_5 nanoribbons and GO nanosheets. The self-assembled V_2O_5/GO gel was isolated from the solution by centrifugation and dried at 80 °C in air for 12 h to form a V_2O_5/GO composite. The V_2O_5/rGO hybrid material was obtained by annealing the V_2O_5/GO composite at 280 °C under nitrogen for 3 h.

2.3. Fabrication of electrodes and symmetric supercapacitors

The electrodes were fabricated by mixing the V_2O_5/rGO hybrid material, super P and poly(vinyldifluoride) (PVDF) at a weight ratio of 70:20:10 in a *N*-methyl-2-pyrrolidone (NMP) solvent. The resulting mixture was pasted onto nickel foam slabs and then dried at 120 °C for 12 h in a vacuum oven to form the electrodes. The areal density of V_2O_5/rGO on the obtained electrodes was about 2 mg cm^{-2}. The symmetric supercapacitors were assembled using two V_2O_5/rGO electrodes sealed in a 2032 coin cells and a 1.0 M Na_2SO_4 aqueous solution as the electrolyte. A filter paper disc was sandwiched between them as the separator.

2.4. Electrochemical measurements

The electrochemical properties of the V_2O_5/rGO electrodes were evaluated in both a three-electrode electrochemical cell and a symmetric coin cell (in form of a supercapacitor) with an electrochemical workstation (IVIUM) at room temperature. For the three-electrode system, the V_2O_5/rGO hybrid electrode was used as the working electrode. A platinum sheet and an Ag/AgCl electrode were used as the counter and reference electrodes, respectively. The electrolyte was a 1.0 M Na_2SO_4 solution. The cyclic voltammetry

(CV) measurement was performed in the potential range from −0.95 to 0.1 V. For the symmetric supercapacitor, the ac-impedance spectrum was measured with a 5.0 mV ac voltage superimposed on the open circuit potential over the frequency range from 10^{-2} to 10^{5} Hz. The CV measurement was performed in the cell potential range from −1.0 to 1.0 V with a scan rate in the range of 10–150 mV s^{-1}. The galvanostatic charge-discharge behavior of the symmetric supercapacitor was measured in the cell potential window from −1.0 to 1.0 V. According to the obtained charge-discharge curve, the specific capacitance of the V_2O_5/rGO hybrid electrode was calculated as

$$C_0 = \frac{2It}{m\Delta V} \quad (1)$$

where C_0 is the specific capacitance (F g^{-1}) of each electrode, I is the discharge current (A), t is the discharge time (s), m is the mass of V_2O_5/rGO material on each electrode (g), and ΔV is the width of the potential window.

The energy and power densities were calculated as

$$E = \frac{0.5C_0\Delta V_w^2}{3.6} \quad (2)$$

$$P_{avg} = \frac{E}{t} \quad (3)$$

$$P_{max} = \frac{(\Delta V_w)^2}{4m\Delta ESR} \quad (4)$$

and

$$ESR = \frac{\Delta V_{IR}}{2I} \quad (5)$$

where E is the energy density (Wh kg^{-1}), ΔV_w is the working potential range (= 1.0 V), P_{avg} is the average power density (W kg^{-1}), t is the discharge time (h), P_{max} is the maximum power density (W kg^{-1}) when measured at matched impedance ($R = ESR$), ESR is the equivalent series resistance (Ω cm^2), and V_{IR} is the IR potential drop when the polarity of the current I was switched during charge-discharge.

2.5. Materials characterization

The surface morphology and microstructure of the materials were examined by a transmission electron microscope (TEM, Hitachi HT7700 operated at 120 kV). X-ray diffraction (XRD) analyses were performed using a Bruker D8 Advance spectrometer with graphite-monochromatized high-intensity Cu Kα radiation. The oxidation states of vanadium in the materials were determined by X-ray photoelectron spectra (XPS), which were collected using a source (PE = 1600 eV) on a Kratos Axis Ultra DLD instrument with monochromatic Al Kα radiation. The Fourier transform infrared spectra (FTIR) were taken out on an Agilent Technologies Cary 630 FTIR spectrometer. Raman spectrum analyses were carried out on a DXR Raman spectrometer (Thermo Scientific) using an excitation laser with a wavelength of 532 nm. The specific surface area (SSA) was calculated by the Brunauer-Emmett-Teller (BET) method from the adsorption branches of isotherms measured with a Quantachrome Autosorb iQ instrument.

3. Results and discussion

The procedure of the microwave-assisted exfoliation method to prepare V_2O_5 nanoribbons from crystalline bulk α-V_2O_5 powder is schematically shown in Fig. 1. To ensure most of the microwave energy was concentrated on the V_2O_5 particles and the adsorbed water molecules during the microwave-assisted exfoliation (i.e. so-called specific heating), THF - an organic solvent with a low microwave-absorbing capability (represented by tanδ, the loss tangent) was chosen as the solvent to prepare the V_2O_5 powder suspension. The tanδ of THF is just 0.042. In contrast, the tanδ values for water and α-V_2O_5 are relatively higher, at 0.123 and ~0.1, respectively [32]. In the first step, the bulk V_2O_5 powder was soaked in water for 4 h to absorb water molecules both on the surface and in the interlayer space of its layered structure. After filtration, the collected V_2O_5 powder was dispersed in THF to form a suspension and then subjected to microwave treatment. During the treatment, due to the interaction of the alternating microwave field with the atoms in the VO_5 layers and the intercalated water molecules, the layered structure were disrupted and exfoliated from the bulk crystals. Meanwhile, the VO_5 layers, which are essentially composed of zigzag double chains of square VO_5 pyramidal units, were broken into nanoribbons because of the relatively weak connection between the double chains [33]. After removing the

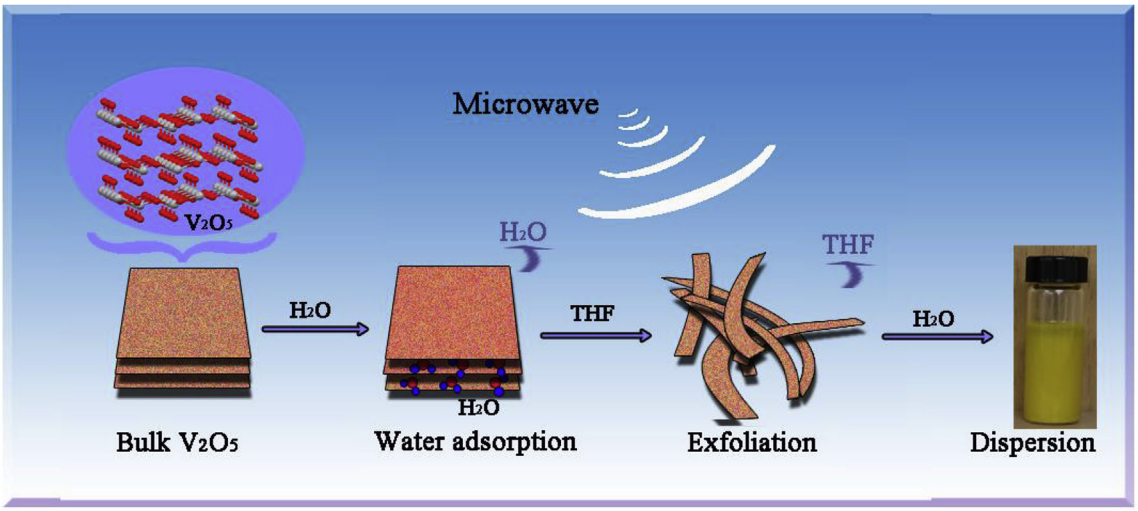

Fig. 1. Schematic procedure for preparation of V_2O_5 nanoribbons by microwave-assisted exfoliation.

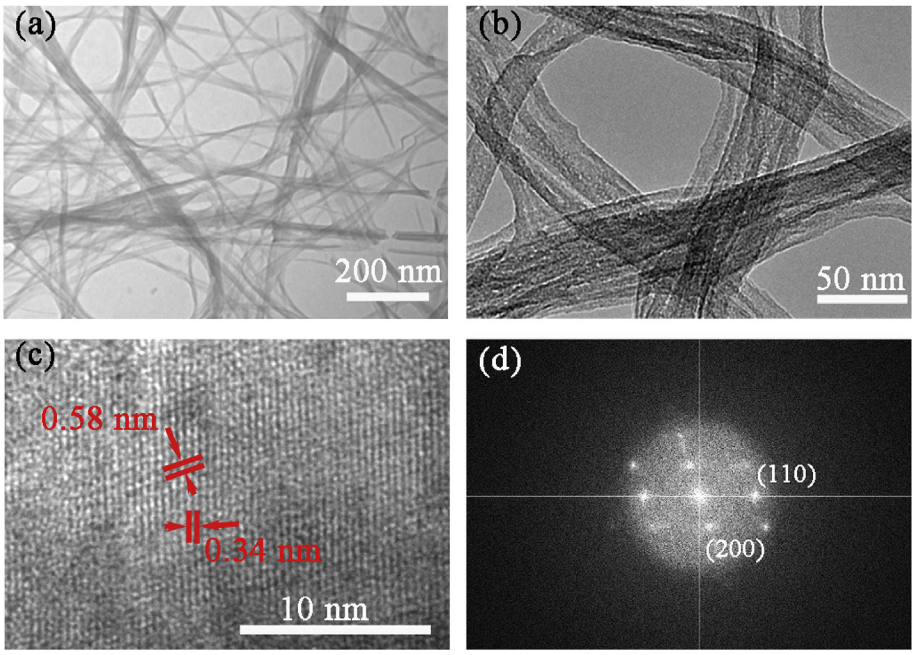

Fig. 2. TEM images (a,b), HRTEM (c) and FFT (d) of the exfoliated V_2O_5 nanoribbons.

THF and washing, the exfoliated powder was dispersed in water and sonicated for 15 min, and then the V_2O_5 nanoribbons were collected from the sonicated dispersion by centrifugation.

Transmission electron microscopy (TEM) was performed to examine the morphology and crystallinity of the exfoliated V_2O_5 nanoribbons. As shown in Fig. 2(a), large quantities of randomly oriented V_2O_5 nanoribbons with a width of 10–50 nm and a length of thousands of nanometres can be found in the exfoliated sample. Fig. 2(b) shows that the obtained nanoribbons are not smooth but present clear wrinkles on the surface. The HRTEM observation (Fig. 2(c)) and the fast Fourier transform (FFT) diffraction pattern (Fig. 2(d)) of the representative nanoribbons illustrate the crystalline nature of the nanoribbons. The interference fringes with d spacings of 0.58 and 0.34 nm correspond to the (200) and (110) planes of the layered α-V_2O_5 structure, respectively. The lattice fringes and FFT pattern shown in Fig. 2(c) and (d) indicate that, while the microwave treatment leads to exfoliation of V_2O_5 into wrinkled nanoribbons, the crystalline characteristics of the VO_5 layers are well preserved.

The structure of the nanoribbons was further surveyed by X-ray diffraction (XRD), Raman spectra, Fourier transform infrared spectra (FTIR) and X-ray photoelectron spectra (XPS) (Fig. 3). For comparison, the analyses were also conducted on a commercial α-V_2O_5 powder, the raw material used for the exfoliation. For the commercial α-V_2O_5 powder, as shown in Fig. 3(a), the characteristic peaks at 15.3°, 20.3°, 21.7°, 26.1°, 31.0°, 32.4°and 34.3° are clearly detected and can be assigned to (200), (001), (101), (110), (301) (011) and (310) planes of the α-V_2O_5 structure (PDF$^{\#}$ 41–1426), respectively. While all V_2O_5 nanosheets by liquid exfoliation exhibit a lamellar structure [30,31], it is interesting that no diffraction peak can be detected from the V_2O_5 nanoribbons produced by the microwave-assisted exfoliation although the lattice fringes can be clearly observed by HRTEM (Fig. 2(c)). This should be attributed to the wrinkled structure of the nanoribbons. As illustrated in Fig. S1, the wrinkled layered structure may lead to incoherent X-ray scattering to different directions and thus no diffraction peak can be detected.

However, the Raman analysis demonstrates that the V_2O_5 nanoribbons and commercial α-V_2O_5 powder exhibit almost the same spectra (Fig. 3(b)). The peaks at Raman shifts of 286.2, 481.0, 525.5, 697.5 and 998.0 cm^{-1} correspond to the V–O1 bending, V–O3 bending, V–O2 stretching, V–O3 stretching and V–O1 stretching of the VO_5 layers in the α-V_2O_5 structure (Fig. S2), respectively [34–36]. These results suggest the arrangement of V and O atoms in the nanoribbons remains intact after the microwave-assisted exfoliation process, in agreement with the observation of HRTEM and FFT pattern. In addition, the nanoribbons and commercial powder also show almost the same FTIR spectra (Fig. 3(c)), while the stronger peaks at about 1623.1 and 3492.7 cm^{-1} can be attributed to the adsorbed water or hydration of the V_2O_5 nanoribbons [37]. The valence state of V in the nanoribbons was analyzed by XPS. As shown in Fig. 3(d), two distinct peaks at 517.3 and 524.8 eV can be detected, corresponding to V $2p_{3/2}$ and V $2p_{1/2}$, respectively, which are consistent with the binding energies expected for V_2O_5 [38]. Compared with the nanosheets exfoliated in water in the literature [31], the nanoribbons in this study exhibit a higher Brunauer-Emmett-Teller (BET) surface area of 40 $m^2 g^{-1}$ (Fig. S3).

The supernatant of V_2O_5 nanoribbons was used to prepare a V_2O_5/rGO hybrid material by a simple self-assembly method based on the electrical double layer and DLVO theories. As demonstrated in Fig. S4, GO nanosheets were easily mixed with the V_2O_5 nanoribbons supernatant to form a stable binary suspension due to electrostatic repulsion by the negative surface charge on the two components. After addition of 0.1 M Na_2SO_4 solution to the suspension, the diffuse electrical double layers on the V_2O_5 nanoribbons and GO nanosheets were compressed by the high concentration of Na^+ ions. The cations also served as bridges to directly increase the attraction between the nanoribbons and nanosheets, and thus the two components assembled to form a V_2O_5/GO composite. Finally, the self-assembled V_2O_5/GO was converted into V_2O_5/rGO hybrid by thermal annealing in nitrogen at 280 °C, which was sufficient to remove a large amount of oxygen-containing groups in GO and convert GO into highly conductive rGO.

The morphology and composition of the as-prepared V_2O_5/rGO

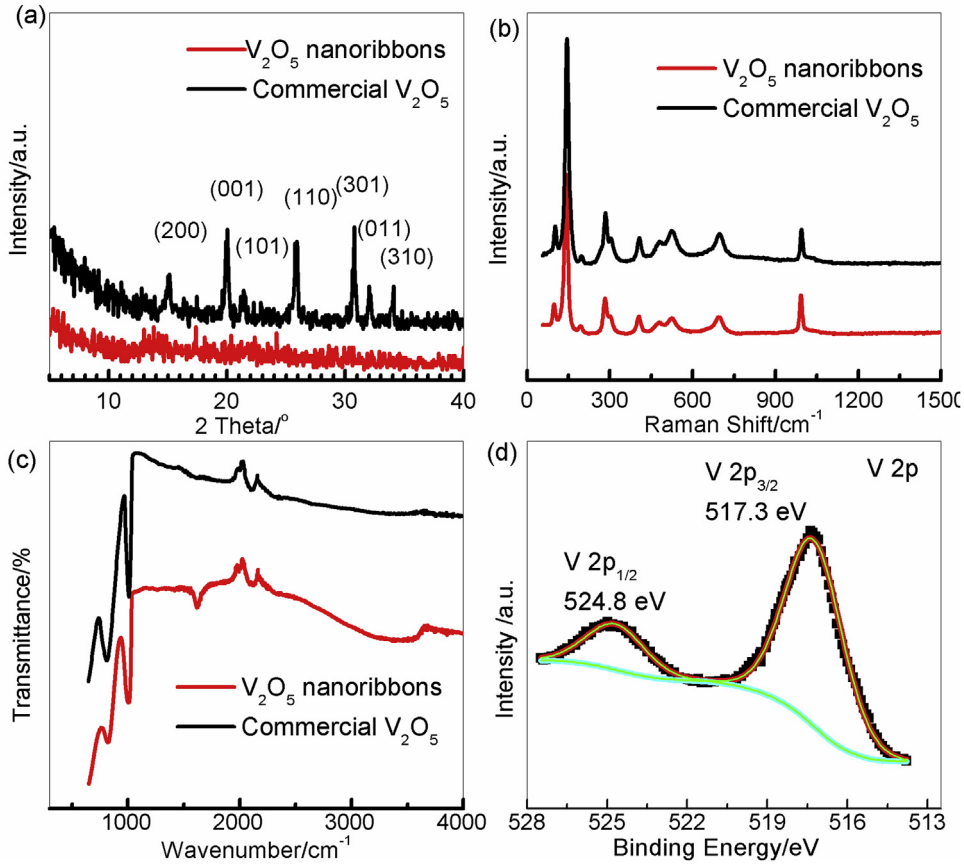

Fig. 3. XRD patterns (a), Raman spectra (b), FTIR spectra (c) and V 2p XPS spectrum (d) of the V_2O_5 nanoribbons.

hybrid were again investigated by TEM, Raman spectra and XPS. Fig. 4(a) confirms that the rGO nanosheets and V_2O_5 nanoribbons are strongly bound together after the assembly and thermal annealing. Numerous V_2O_5 nanoribbons cover the surface of larger rGO nanosheets. The Raman spectra of the as-prepared V_2O_5/rGO and the corresponding V_2O_5/GO (Fig. 4(b)) demonstrate that the thermal annealing in nitrogen at 280 °C can dramatically reduce the intensities of the peaks at 286.2 and 998.0 cm^{-1} and increase the ratio of D to G band from 66/103 to 56/58, suggesting that the V_2O_5 nanoribbons in the V_2O_5/GO are partially reduced by the surface functional groups of GO while the GO is converted into rGO due to the oxidation and dissociation of the functional groups during the thermal annealing [35,39]. For example, the carboxyl groups may dissociate into carbon dioxide as follows:

$$HOOC - R - COOH + V_2O_5 \rightarrow R + 2VO_2 + 2CO_2 + H_2O \qquad (6)$$

where R represents the carbon skeleton of GO. These results can be further confirmed by XPS analyses. As illustrated in Fig. 4(c) and (d), the V 2p spectrum of the annealed composite shows that 36.2% of V^{5+} is reduced to V^{4+} (corresponding to signals at 516.4 and 523.5 eV) while the C 1s spectrum exhibits rGO features with a large peak consisting overlapped C—C and C═C peaks and two small C—O and C═O peaks [38,40,41].

The electrochemical performance of the as-prepared V_2O_5/rGO hybrid material was primarily evaluated by cyclic voltammetry (CV) using a three-electrode system. As shown in Fig. S5, the electrode shows rectangular CV curves over the potential range of −0.95—0.1 V (vs. Ag/AgCl), indicating nearly ideal capacitive behavior over this potential range [42]. Furthermore, as the CV scan rate increases from 10 to 100 mV s^{-1}, the response current increases linearly while the shape of the CV curves remains rectangular, suggesting that good high-rate performance can be obtained from the V_2O_5/rGO hybrid material. Considering the fact that most of the V_2O_5 nanowires or nanorods anchored on graphene just exhibit extrinsic supercapacitor or battery-like behavior [16—18], the capacitive behavior of the V_2O_5/rGO hybrid material should be attributed to its distinctive structure. First, the V_2O_5 nanoribbons are derived from the microwave-assisted exfoliation of layered V_2O_5, which makes most of the metal centers that contribute to Faradaic pseudocapacitance to be located on the surface of the oxide, and thus the surface areas available for non-insertion charge storage are dramatically enhanced [43]. More importantly, even though the nanoribbon comprises several VO_5 layers, the wrinkled structure (illustrated in Fig. S1) can provide more facile diffusion paths for charge-compensating ions and thus the intercalation reaction can occur faster and more smoothly compared with the bilayer structures of the V_2O_5 nanorods or nanowires synthesized by hydrothermal methods [44]. In addition, it is well known that the surface chemistry can profoundly influence the capacitive behavior of a material. As shown in Fig. 4(d), there are still some oxygen-containing functional groups on the rGO after thermal annealing. The reactions between the V_2O_5 nanoribbons and GO occurred in the thermal annealing process may play a key role in arranging the functional groups and the ratio of V^{5+} to V^{4+}, which partially contribute to the capacitive behavior of the hybrid material [45—47].

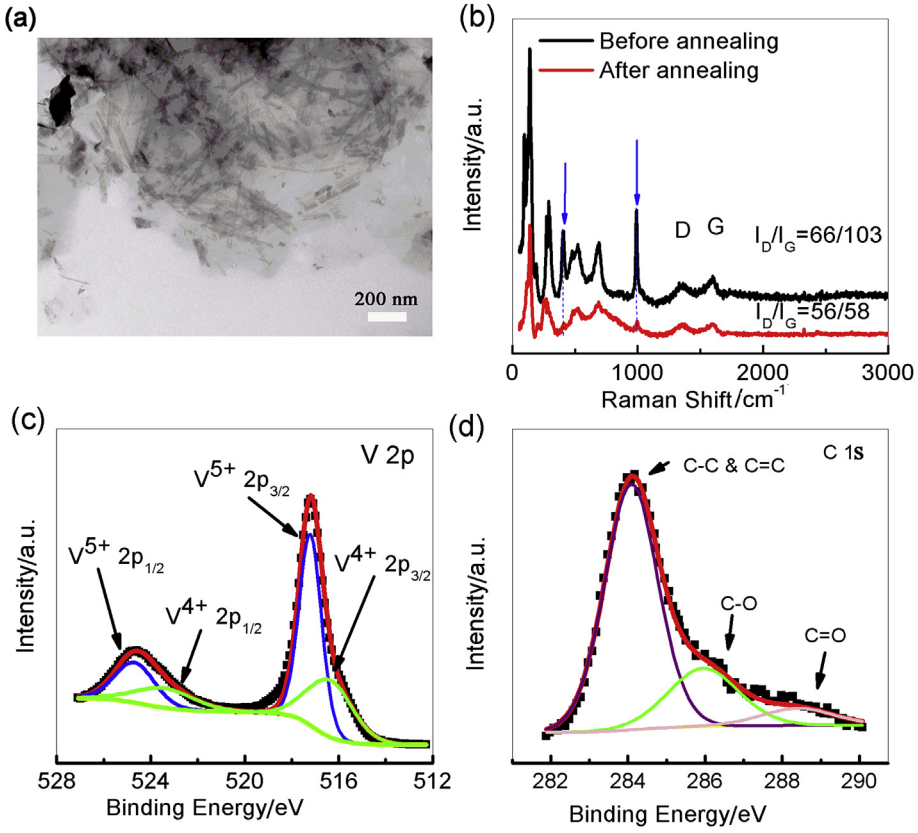

Fig. 4. TEM image (a), Raman spectra (b), V 2p (c) and C 1s (d) XPS spectra of the V_2O_5/rGO hybrid material.

To further evaluate the electrochemical performance of the V_2O_5/rGO hybrid material, CV, galvanostatic charge-discharge and impedance tests were performed on symmetric two-electrode supercapacitors using the V_2O_5/rGO hybrid material as the electrode material and a 1.0 M Na_2SO_4 solution as the electrolyte, respectively. The nearly rectangular CV curves and linear charge-discharge profiles (Fig. 5(a) and (b)) indicate again the typical capacitive behavior of the hybrid material [42,43]. Fig. 5(c) shows the specific capacitances of the V_2O_5/rGO hybrid material at different charge-discharge rates. The specific capacitances are 423.6 and 230 F g^{-1} at 1.0 and 10 A g^{-1}, respectively, which are consistent with the CV results measured with the 3-electrode system (Fig. S5(b)). To further elaborate the energy and power densities, a Ragone plot is displayed in Fig. 5(d). The V_2O_5/rGO hybrid material delivers a high energy density of 58.8 Wh kg^{-1} at an average power density of 500 W kg^{-1} (corresponding to the maximum power density of 21 kW kg^{-1}). At a much higher average power density of 5 kW kg^{-1} (corresponding to the maximum power density of 24 kW kg^{-1}), the energy density can still remain as high as 32 Wh kg^{-1}. This result indicates the outstanding high-energy and high-rate capability of the V_2O_5/rGO hybrid material compared with those reported in the recent literature [18,48–50], which are attributed to its unique structure. The thin nanoribbon architecture can shorten the solid-diffusion distance for charge-compensating ions in the V_2O_5 component while the rGO nanosheets serve as highly conductive paths for electron transport. Furthermore, although the V_2O_5 nanoribbons and the rGO nanosheets are strongly stacked, the wrinkled structure of the V_2O_5 nanoribbons can still provide facile diffusion paths for ions and thus make more reactive sites available in the electrode. These attractive features also enable the V_2O_5/rGO hybrid material to exhibit a remarkable cycling stability at the current density of 5 A g^{-1}. As shown in Fig. 5(e), the capacitance only decreases by 20% during the initialization stage in the first 200 cycles and then remains almost the same over the subsequent 1800 cycles. The impedance spectra (Fig. 5(f)) show that the charge-transfer résistance only increases slightly from 2.1 to 5.7 Ω during the cycling process, consistent with the good cycling stability.

4. Conclusion

A novel processing technique based on specific microwave heating was successfully developed to exfoliate crystalline α-V_2O_5 powders into wrinkled V_2O_5 nanoribbons. The as-prepared V_2O_5 nanoribbons were further used to form a strongly bound V_2O_5/rGO hybrid material through a simple cation-mediated self-assembly process followed by thermal annealing treatment. The yield of the nanoribbons can reach up to 20% after 40 min of microwave treatment, and the V_2O_5/rGO hybrid material exhibits typical capacitive behavior in the potential range from −0.95 to 0.1 V with a specific capacitance of 423.6 F g^{-1} at 1 A g^{-1}. The symmetric supercapacitor assembled with the hybrid material shows a high energy density of 58.8 Wh kg^{-1} at an average power density of 500 W kg^{-1}, and an excellent high-rate capability with an energy density of 32 Wh kg^{-1} at 5 kW kg^{-1}. In addition, the V_2O_5/rGO hybrid material exhibits superior cycling stability with the specific capacitance remaining nearly constant up to 1800 charge-discharge cycles after the initialization in the first 200 cycles. These properties are attributed to the highly dispersed wrinkled V_2O_5 nanoribbons supported by the highly conductive rGO templates. These results show the great potential of the microwave-assisted technique for

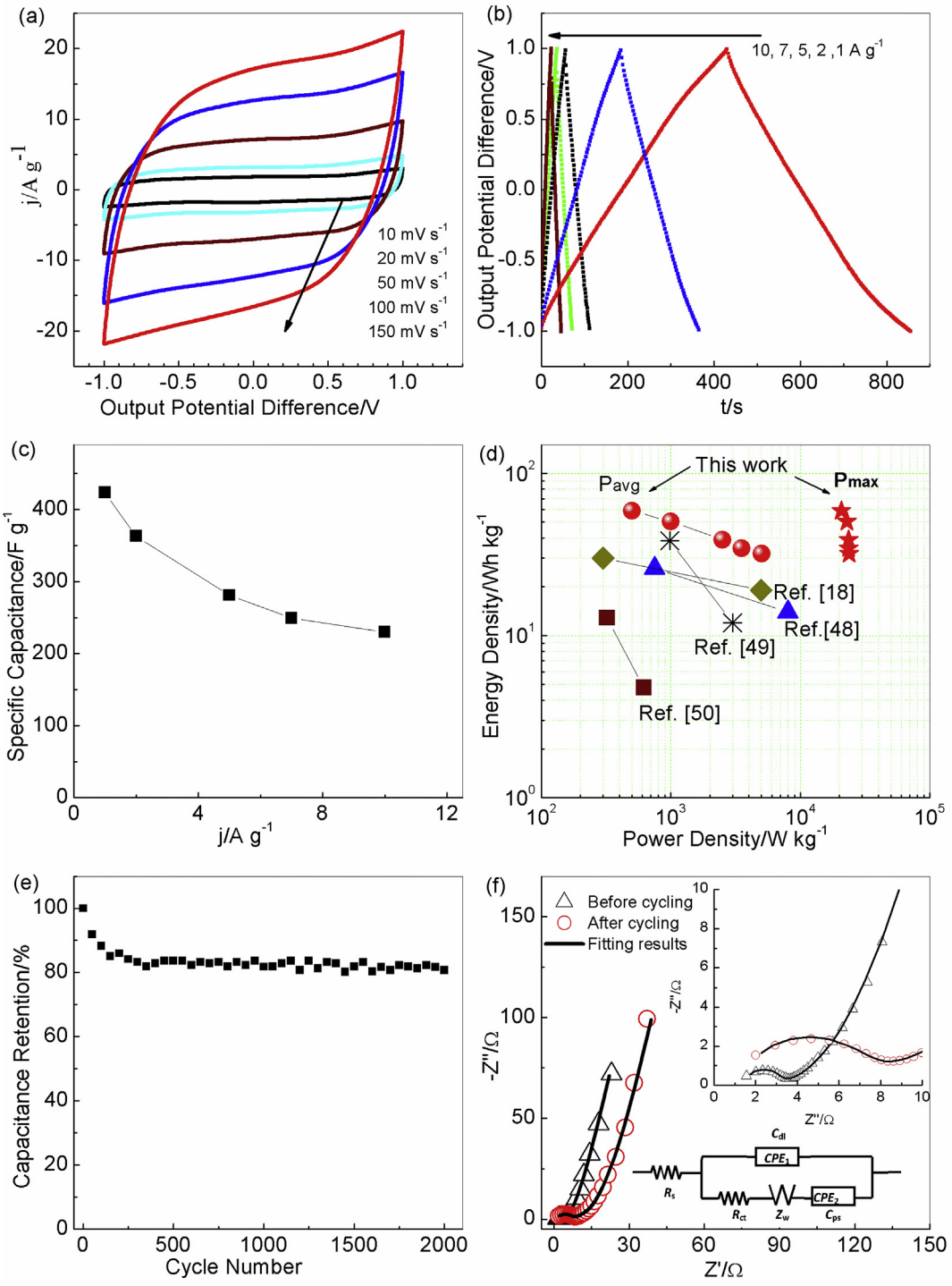

Fig. 5. CV curves (a), charge-discharge curves (b), specific capacitance vs. current density curve (c), Ragone plot (d), cycling performance at 5 A g^{-1} (e), and impedance spectra (f) of the symmetric supercapacitor assembled with the V_2O_5/rGO electrodes.

high-yield production of V_2O_5 nanoribbons toward future scalable electrical energy storage applications.

Acknowledgements

The authors thank Mr. A. Elangovan and Dr. A. Nepal for assistance in TEM and BET data acquisition, respectively. Dr. Y. Chen acknowledges the financial supports of the National Natural Science Foundation of China (Grant No. 51374252) and the China Scholarship Council (Grant No. 201706375089). Dr. J. Li acknowledges the support in materials synthesis/characterization and electrochemical tests by a grant DMR-1707585 from US National Science Foundation. The XPS measurements were carried out at the University of Nebraska Center for Materials and Nanoscience (NCMN) which is a part of the nationwide NNCI network supported by NSF.

Appendix A. Supplementary data

Supplementary data to this article can be found online at https://doi.org/10.1016/j.electacta.2019.135200.

References

[1] Y. Shao, M.F. El-Kady, J. Sun, Y. Li, Q. Zhang, M. Zhu, H. Wang, B. Dunn, R.B. Kaner, Chem. Rev. 118 (2018) 9233.
[2] V. Augustyn, P. Simon, B. Dunn, Energy Environ. Sci. 7 (2014) 1597.
[3] C.P. Grey, J.M. Tarascon, Nat. Mater. 16 (2017) 45.
[4] P. Simon, Y. Gogotsi, Nat. Mater. 7 (2008) 845.
[5] W. Chen, R.B. Rakhi, L. Hu, X. Xie, Y. Cui, H.N. Alshareef, Nano Lett. 11 (2011) 5165.
[6] J. Yan, Q. Wang, T. Wei, Z. Fan, Adv. Energy Mater. 4 (2014), 1300816.
[7] N. Choudhary, C. Li, J. Moore, N. Nagaiah, L. Zhai, Y. Jung, J. Thomas, Adv. Mater. 29 (2017) 1605336.
[8] X. Lu, C. Wang, F. Favier, N. Pinna, Adv. Energy Mater. 7 (2017), 1601301.
[9] P. Yang, Y. Ding, Z. Lin, Z. Chen, Y. Li, P. Qiang, M. Ebrahimi, W. Mai, C.P. Wong, Z.L. Wang, Nano Lett. 14 (2014) 731.
[10] X. Tang, R. Jia, T. Zhai, H. Xia, ACS Appl. Mater. Interfaces 7 (2015) 27518.
[11] S. Cho, J. Kim, Y. Jo, A.T.A. Ahmed, H.S. Chavan, H. Woo, A.I. Inamdar, J.L. Gunjakar, S.M. Pawar, Y. Park, H. Kim, H. Im, J. Alloy. Comp. 725 (2017) 108.
[12] Y. Chen, J.-H. Guan, H. Gan, B.-Z. Chen, X.-C. Shi, J. Appl. Electrochem. 48 (2018) 105.
[13] A. Roy, A. Ray, S. Saha, M. Ghosh, T. Das, B. Satpati, M. Nandi, S. Das, Electrochim. Acta 283 (2018) 327.
[14] Y. Chen, H. Gan, J.-H. Guan, L.-T. Cao, J. Alloy. Comp. 760 (2018) 6.
[15] V.D. Nithya, N.S. Arul, J. Power Sources 327 (2016) 297.
[16] W. Sun, G. Gao, Y. Du, K. Zhang, G. Wu, J. Mater. Chem. 6 (2018) 9938.
[17] B. Saravanakumar, K.K. Purushothaman, G. Muralidharan, J. Electroanal. Chem. 758 (2015) 111.
[18] L. Yao, C. Zhang, N. Hu, L. Zhang, Z. Zhou, Y. Zhang, Electrochim. Acta 295 (2019) 14.
[19] Z. Liu, H. Zhang, Q. Yang, Y. Chen, Electrochim. Acta 287 (2018) 149.
[20] A. Elmouwahidi, E. Bailón-García, A.F. Pérez-Cadenas, N. Fernández-Sáez, F. Carrasco-Marín, Adv. Funct. Mater. 28 (2018), 1802337.
[21] J. Liu, J. Essner, J. Li, Chem. Mater. 22 (2010) 5022.
[22] S.A. Klankowski, G.P. Pandey, G. Malek, C.R. Thomas, S.L. Bernasek, J. Wu, J. Li, Nanoscale 7 (2015) 8485.
[23] Y. Zhu, L. Peng, Z. Fang, C. Yan, X. Zhang, G. Yu, Adv. Mater. 30 (2018), 1706347.
[24] C. Tan, X. Cao, X.-J. Wu, Q. He, J. Yang, X. Zhang, J. Chen, W. Zhao, S. Han, G.-H. Nam, M. Sindoro, H. Zhang, Chem. Rev. 117 (2017) 6225.
[25] Q. Weng, X. Wang, X. Wang, Y. Bando, D. Golberg, Chem. Soc. Rev. 45 (2016) 3989.
[26] X. Huang, Z. Zeng, H. Zhang, Chem. Soc. Rev. 42 (2013) 1934.
[27] M. Osadaab, T. Sasaki, J. Mater. Chem. 19 (2009) 2503.
[28] R. Ma, T. Sasaki, Acc. Chem. Res. 48 (2015) 136.
[29] Y. Wang, K. Takahashi, K. Lee, G. Cao, Adv. Funct. Mater. 16 (2016) 1133.
[30] X. Rui, Z. Lu, H. Yu, D. Yang, H.H. Hng, T.M. Lim, Q. Yan, Nanoscale 5 (2013) 556.
[31] C. Zhang, S.-H. Park, S.E. O'Briena, A. Seral-Ascaso, M. Liang, D. Hanlon, D. Krishnan, A. Crossley, N. McEvoy, J.N. Coleman, V. Nicolosi, Nano Energy 39 (2017) 151.
[32] Y.-J. Zhu, F. Chen, Chem. Rev. 114 (2014) 6462.
[33] A. Shimizu, T. Watanabe, M. Inagaki, J. Mater. Chem. 4 (1994) 1475.
[34] R. Baddour-Hadjean, M.B. Smirnov, K.S. Smirnov, V. Yu Kazimirov, J.M. Gallardo-Amores, U. Amador, M.E. Arroyo-de Dompablo, J.P. Pereira-Ramos, Inorg. Chem. 51 (2012) 3194.
[35] F. Urena-Begara, A. Crunteanu, J.-P. Raskin, Appl. Surf. Sci. 403 (2017) 717.
[36] S. Thiagarajan, M. Thaiyan, R. Ganesan, RSC Adv. 6 (2016) 82581.
[37] I. Mjejri, N. Etteyeb, F. Sediri, Mater. Res. Bull. 48 (2013) 3335.
[38] E. Hryha, E. Rutqvist, L. Nyborg, Surf. Interface Anal. 44 (2012) 1022.
[39] X. Dıez-Betriu, S. Alvarez-Garcia, C. Botas, P. Alvarez, J. Sanchez-Marcos, C. Prieto, R. Menendez, A. Andres, J. Mater. Chem. C 1 (2013) 6905.
[40] I. Sengupta, S. Chakraborty, M. Talukdar, J. Mater. Res. 33 (2018) 4113.
[41] Q. Xie, P. Liu, D. Zeng, W. Xu, L. Wang, Z.-Z. Zhu, L. Mai, D.-L. Peng, Adv. Funct. Mater. 28 (2018), 1707433.
[42] P. Simon, Y. Gogotsi, B. Dunn, Science 343 (2014) 1210.
[43] Y. Gogotsi, R.M. Penner, ACS Nano 12 (2018) 2081.
[44] M. Vujković, B.S. Paunković, I.S. Simatović, M. Mitrić, C.A.C. Sequeira, S. Mentusa, Electrochim. Acta 147 (2014) 167.
[45] Z. Jovanović, D. Bajuk-Bogdanović, S. Jovanović, Z. Mravik, J. Kovać, I. Holclajtner-Antunović, M. Vujković, Electrochim. Acta 258 (2017) 1228.
[46] Z. Jovanović, I. Holclajtner-Antunović, D. Bajuk-Bogdanović, S. Jovanović, Z. Mravik, M. Vujković, Electrochem. Commun. 83 (2017) 36.
[47] Y. Chen, W. Hu, H. Gan, J.-W. Wang, X.-C. Shi, Electrochim. Acta 246 (2017) 890.
[48] J. Guo, Q. Zhang, Q. Li, J. Sun, C. Li, B. He, Z. Zhou, L. Xie, M. Li, Y. Yao, ACS Appl. Mater. Interfaces 10 (2018) 29705.
[49] N.M. Ndiaye, B.D. Ngom, N.F. Sylla, T.M. Masikhwa, M.J. Madito, D. Momodu, T. Ntsoane, N. Manyala, J. Colloid Interface Sci. 532 (2018) 395.
[50] B. Saravanakumar, K.K. Purushothaman, G. Muralidharan, Microporous Mesoporous Mater. 258 (2018) 83.